



Single-cell spatial landscape of immunotherapy response reveals mechanisms of CXCL13 enhanced antitumor immunity

Mark Sorin,^{1,2} Elham Karimi,¹ Morteza Rezanejad,³ Miranda W Yu,^{1,4} Lysanne Desharnais,^{1,2} Sheri A C McDowell,^{1,4} Samuel Doré,^{1,2} Azadeh Arabzadeh,¹ Valerie Breton,¹ Benoit Fiset ,¹ Yuhong Wei,¹ Roni Rayes,¹ Michele Orain,⁵ Francois Coulombe,⁵ Venkata S K Manem,⁵ Andreanne Gagne,⁵ Daniela F Quail,^{1,4,6} Philippe Joubert,⁵ Jonathan D Spicer,^{1,7} Logan A Walsh ^{1,2}

To cite: Sorin M, Karimi E, Rezanejad M, *et al.* Single-cell spatial landscape of immunotherapy response reveals mechanisms of CXCL13 enhanced antitumor immunity. *Journal for ImmunoTherapy of Cancer* 2023;**11**:e005545. doi:10.1136/jitc-2022-005545

► Additional supplemental material is published online only. To view, please visit the journal online (<http://dx.doi.org/10.1136/jitc-2022-005545>).

MS and EK contributed equally.

MS and EK are joint first authors.

Accepted 13 December 2022



© Author(s) (or their employer(s)) 2023. Re-use permitted under CC BY-NC. No commercial re-use. See rights and permissions. Published by BMJ.

For numbered affiliations see end of article.

Correspondence to

Dr Logan A Walsh;
logan.walsh@mcgill.ca

Dr Jonathan D Spicer;
jonathan.spicer@mcgill.ca

ABSTRACT

Background Immunotherapy has revolutionized clinical outcomes for patients suffering from lung cancer, yet relatively few patients sustain long-term durable responses. Recent studies have demonstrated that the tumor immune microenvironment fosters tumorous heterogeneity and mediates both disease progression and response to immune checkpoint inhibitors (ICI). As such, there is an unmet need to elucidate the spatially defined single-cell landscape of the lung cancer microenvironment to understand the mechanisms of disease progression and identify biomarkers of response to ICI.

Methods Here, in this study, we applied imaging mass cytometry to characterize the tumor and immunological landscape of immunotherapy response in non-small cell lung cancer by describing activated cell states, cellular interactions and neighborhoods associated with improved efficacy. We functionally validated our findings using preclinical mouse models of cancer treated with anti-programmed cell death protein-1 (PD-1) immune checkpoint blockade.

Results We resolved 114,524 single cells in 27 patients treated with ICI, enabling spatial resolution of immune lineages and activation states with distinct clinical outcomes. We demonstrated that CXCL13 expression is associated with ICI efficacy in patients, and that recombinant CXCL13 potentiates anti-PD-1 response in vivo in association with increased antigen experienced T cell subsets and reduced CCR2+ monocytes.

Discussion Our results provide a high-resolution molecular resource and illustrate the importance of major immune lineages as well as their functional substates in understanding the role of the tumor immune microenvironment in response to ICIs.

BACKGROUND

Immune checkpoint inhibitors (ICI) have transformed cancer care across a range of solid malignancies including non-small cell lung cancer (NSCLC). Despite the identification of several correlative biomarkers of

WHAT IS ALREADY KNOWN ON THIS TOPIC

⇒ Immune checkpoint inhibitors (ICI) have revolutionized the cancer treatment, but durable responses are rare and challenging to predict.

WHAT THIS STUDY ADDS

⇒ Here, in this study, we use highly-multiplexed imaging mass cytometry to define the spatial immune landscape of non-small cell lung cancer associated with ICI response.

HOW THIS STUDY MIGHT AFFECT RESEARCH, PRACTICE OR POLICY

⇒ Our findings identify key features within the tumor immune microenvironment that may underlie ICI response and demonstrate how CXCL13 augments anti-programmed cell death protein-1 efficacy.

response such as programmed cell death-ligand 1 (PD-L1) expression and tumor mutational burden, real-world data show that the majority of patients with NSCLC will not respond to ICI.^{1,2} This is the result of a multitude of resistance mechanisms that include, but are not limited to, aberrations in tumor neoantigen burden, effector T-cell infiltration, epigenetic modulation, T-cell exhaustion, the microbiome, and abnormal neovascularization.^{3,4} As such, there is a clear unmet need to understand the biology underlying ICI efficacy and identify strategies to potentiate ICI response.

Both the nature and level of immune infiltrate within tumors have been shown to have important implications in the downstream response to ICIs.^{5,6} Antitumoral immunity requires highly organized, spatially coordinated localization of immune cells within the tumor microenvironment and the ability to

resolve these interactions is critical to understand their behavior. Pioneering studies have recently provided a framework for interrogating complex cellular interactions that mediate tumor evolution and response to therapy. For example, topological single-cell network analyses of the cellular architecture of breast cancer,⁷⁻⁹ colorectal cancer¹⁰ and pancreatic cancer¹¹ have revealed multicellular spatial features of the tumor microenvironment associated with clinical outcomes. High dimensional imaging has also been applied to understand the mechanisms of therapeutic efficacy in cancer, including anti-HER2¹² or anti-cytotoxic T-lymphocytes-associated protein 4/programmed cell death protein-1 (PD-1) in melanoma.¹³ In lung cancer, although significant progress has been made to highlight the dynamic tumor immune microenvironment (TIME) using single-cell technologies,¹⁴⁻¹⁷ spatially-resolved single-cell imaging data sets are scarce. To address this knowledge gap, here, in this study, we perform highly multiplexed imaging mass cytometry to interrogate the single-cell spatial landscape of response to ICI in NSCLC.

METHODS

Patient cohort

Using RECIST 1.1 (Response Evaluation Criteria in Solid Tumours), response to treatment was defined as stable disease or partial/complete response at least 6 months after the initiation of immunotherapy, while absence of response was defined as progressing disease within 6 months following initiation of the treatment. We used a cohort of successive patients that underwent an immunotherapy treatment upon recurrence and had given their consent to the biobank for the use of their clinical data and surgery, biopsy or cytology specimen (from primary lung tumor or metastases). Cases with a sufficient amount of tumor and adequate tissue quality were included in the tissue microarray (TMA) block. The pathologist who built the TMA was blinded to the response status of the patients and thus no bias was introduced in terms of selecting responders and non-responders. TMA was constructed by selecting one 1.0mm core from the surgical tumor specimen or biopsy from both responder and non-responder groups. Clinicopathological information for our cohort can be found in online supplemental tables 1,2.

Sample staining and IMC antibody panel

An imaging mass cytometry (IMC) antibody panel was designed to include 14 cell lineage markers, 11 co-stimulatory/inhibitory markers, 6 immune signaling markers and four tissue structural markers. Clone information is available in online supplemental table 3. Previous optimization was done for 19 out of 35 antibodies.¹⁸ The remaining antibodies were either purchased pre-conjugated (Fluidigm) or conjugated to metal isotopes by the Single Cell and Imaging Mass Cytometry Platform at the Goodman Cancer Institute (McGill University), using Maxpar Conjugation Kits as per the manufacturer's

protocol (Fluidigm). Multiple control tissues were included during optimization, including appendix, placenta, normal lung, spleen, tonsil and thymus, to enable evaluation of expected staining patterns. Staining and incubation were performed using a Ventana Discovery Ultra auto-stainer platform (Roche Diagnostics). Briefly, formalin-fixed paraffin-embedded (FFPE) slides were incubated in EZ Prep solution to allow for deparaffinization at 70°C, followed by antigen-retrieval at 95°C using standard Cell Conditioning 1 solution. Slides were then removed from the machine, rinsed with 1× phosphate-buffered saline (PBS), and incubated in Dako Serum-free Protein Block solution for 45 min prior to applying a cocktail containing the metal-tagged antibodies in Dako Antibody Diluent overnight at 4°C. Slides were washed with 0.2% Triton X and 1× PBS, and then incubated with the metal-conjugated anti-biotin antibody in Dako Antibody Diluent (1 hour, room temperature (RT)). Slides were once again washed with 0.2% Triton X and 1× PBS, counterstained with Intercalator-Ir (1:400 in 1× PBS, 30 min at RT), rinsed with distilled water (5 min) and air-dried. Acquisition was performed with a Hyperion Imaging System and Fluidigm commercial acquisition software (Fluidigm). A frequency of 200Hz was used to laser-ablate the cores at a resolution of roughly 1 μm, and for our cohort, laser power was used at instrumental setting '3'. A 1 mm² area (approximate size of one core) required approximately 2 hours of run time. Note, while all markers adequately stained control tissue, for a few markers, we were not confident in the accuracy of staining in every core across our entire lung adenocarcinoma cohort, and thus these markers were not used for downstream interpretation (CD39, CD40, TIM3, B7H4, VISTA, CCR7, CCR5, PD-1). Representative images of each antibody in control tissues are included in online supplemental figure S1a.

Cell segmentation and lineage assignment

We first segmented cells using a novel cell segmentation pipeline. The details can be found using the following link: <https://biorxiv.org/cgi/content/short/2022.02.27.482183v1>. To evaluate the existence of a marker at a particular location, we created a multilevel image stack based on staining intensity for each marker where each mask/level within the stack is generated using k-means clustering¹⁹ and a mixture of generalized gaussian models.²⁰ To overcome challenges related to signal-to-noise ratio and to extract markers with low expression we considered six levels for each marker in our panel and the appropriate mask was subsequently manually curated for each marker. For each mask:

1. A median filter with a particular window size (3×3) is used to convolve the grayscale image.
2. The k-means algorithm is used to cluster each pixel in the image into six groups of intensity levels.
3. All groups up to a particular intensity level are considered as foreground (1) and the rest as background (0) for each channel.

- To both avoid noisy regions and obtain smoother binary masks, we applied a morphological blob removal process where binary blobs of a particular area are removed from masks.
- An additional binary mask obtained using the adaptive binarization method with a sensitivity of 0.4 was used as a channel-specific morphological operation. The mask is then amalgamated with the mask obtained in step 4. This process allows to improve the accuracy of select markers.

We considered the curated mask for each lineage marker M_k across each cell c_i , where $k = 1, \dots, n$ and n is the number of lineage markers. Let us assume that $p_{c_i}^j$ is the j^{th} pixel that lies in the surrounding of c_i and each pixel has the following presence vector based on the lineage markers:

$$E(p_{c_i}^j) = \{p_{M_1}^j, p_{M_2}^j, \dots, p_{M_n}^j\}$$

where $p_{M_i} = \{0 \text{ or } 1\}$ determines whether the pixel $p_{c_i}^j$ is positive for a particular marker. To assess whether each pixel within a cell is positive or negative for a select marker, we determined the majority vector by summing over the presence of all vectors as:

$$M_{c_i} = \left\{ \sum_{j=1}^{N_{c_i}} p_{M_1}^j, \sum_{j=1}^{N_{c_i}} p_{M_2}^j, \dots, \sum_{j=1}^{N_{c_i}} p_{M_n}^j \right\}$$

where N_{c_i} is the number of pixels in the cell c_i . The maximum value in vector M_{c_i} is used for cell type assignment. Cell lineages are assigned in hierarchical rank priority order (figure 1B).

Costimulatory/inhibitory marker analysis

We first calculated the mean staining intensity for each antibody in all 16 cell lineages. We then calculated the Z-score for each marker across all cell lineages. For comparison between responders and non-responders, we only evaluated cell lineages with a Z-score >1 . The justification for this approach is that with very low staining intensity, the relative staining intensity in responders compared with non-responders can seem inflated (eg, a staining intensity of 0.2 vs 1 will give a fivefold relative increase for potentially background staining of a marker for a given cell type). These results can be visualized in figure 1G.

Cell-cell pairwise interaction analysis

To identify significant pairwise interaction/avoidance between cells, we performed a permutation-test-based analysis of spatial single-cell interactions.²¹ P values less than 0.01 were deemed significant. Interacting cells were defined as those within six pixels (6 μm).

Neighborhood identification

Cellular neighborhoods were generated by employing a 'window' capture strategy. The window was composed of the 10 cells in closest proximity to a given cell as previously described.²² A window can be defined as a frequency vector containing the types of X (as indicated) closest cells to a given cell. The window vectors are computed for each cell. Cells were then clustered using scikit-learn,

a software machine learning library for Python, and MiniBatchKMeans clustering algorithm V.0.24.2 with default batch size=100 and random_state=0. Windows were clustered based on cellular composition into seven cellular neighborhoods using MiniBatchKMeans clustering algorithm with $k=7$. Every cell is allocated to a cellular neighborhood based on their defining window vector. The counts of cells within each neighborhood were compared between responders and non-responders.

T-distributed stochastic neighbor embedding

Plots were generated in MATLAB (V.2019b- default parameters). Expression data were normalized to the 95th percentile for visualization purposes.

Cell lines

All cell lines were cultured in DMEM (Dulbecco's Modified Eagle's Medium) media supplemented with 1% penicillin and streptomycin and 10% fetal bovine serum. LLC1 and B16-F10 cell lines were purchased from The American Type Culture Collection. HKP1 and MC38 cells were generous gifts from V Mittal and N Beauchemin, respectively. MC38 cells were passaged in vivo as previously described.²³

Animal models

Animal protocols were approved by the McGill University Animal Care Committee (MCGL-7953) and in line with the standards set by the Canadian Council on Animal Care. Mice were housed in pathogen-free conditions. C57BL/6 male mice were injected subcutaneously with 5×10^5 HKP1 cells, 3×10^5 MC38 cells, 5×10^5 LLC1 cells or 5×10^3 B16-F10 cells resuspended in 1:1 Matrigel:PBS at 5–7 weeks of age. Recombinant CXCL13 (Peprotech; rCXCL13) was administered at 1.25 μg peritumorally per mouse on the day the tumors became palpable (between day 4–6 post-injection, depending on the cell line). The rCXCL13 was administered every 2 days thereafter, until the trial endpoint was reached. Anti-PD-1 (InVivoPlus – BioXcell; clone: J43) and IgG (non-reactive polyclonal Armenian hamster Ab) (InVivoPlus – BioXcell; clone: NA) were resuspended in pH 7.0 dilution buffer (InVivoPure – BioXcell) at a concentration of 10 mg/kg per mouse and injected intraperitoneally 2 days after tumors became palpable. The injections were repeated every 3 days until the endpoint was reached. Weight was monitored once weekly and tumor volume was measured via caliper two to three times weekly once the tumors became palpable.

Immunohistochemistry

Three 6-week-old treatment naïve C57BL/6 male mice were injected in the flank with 5×10^5 HKP1, 3×10^5 MC38 or 5×10^5 LLC1 resuspended in 1:1 Matrigel:PBS. FFPE sections (4 μm) were prepared for each sample and subjected to routine H&E staining. Immunohistochemistry directed against alpha-CD8 (Abcam; clone: EPR21769; 1:500 dilution) was performed on FFPE slides on a Ventana BenchMark XT automated system.

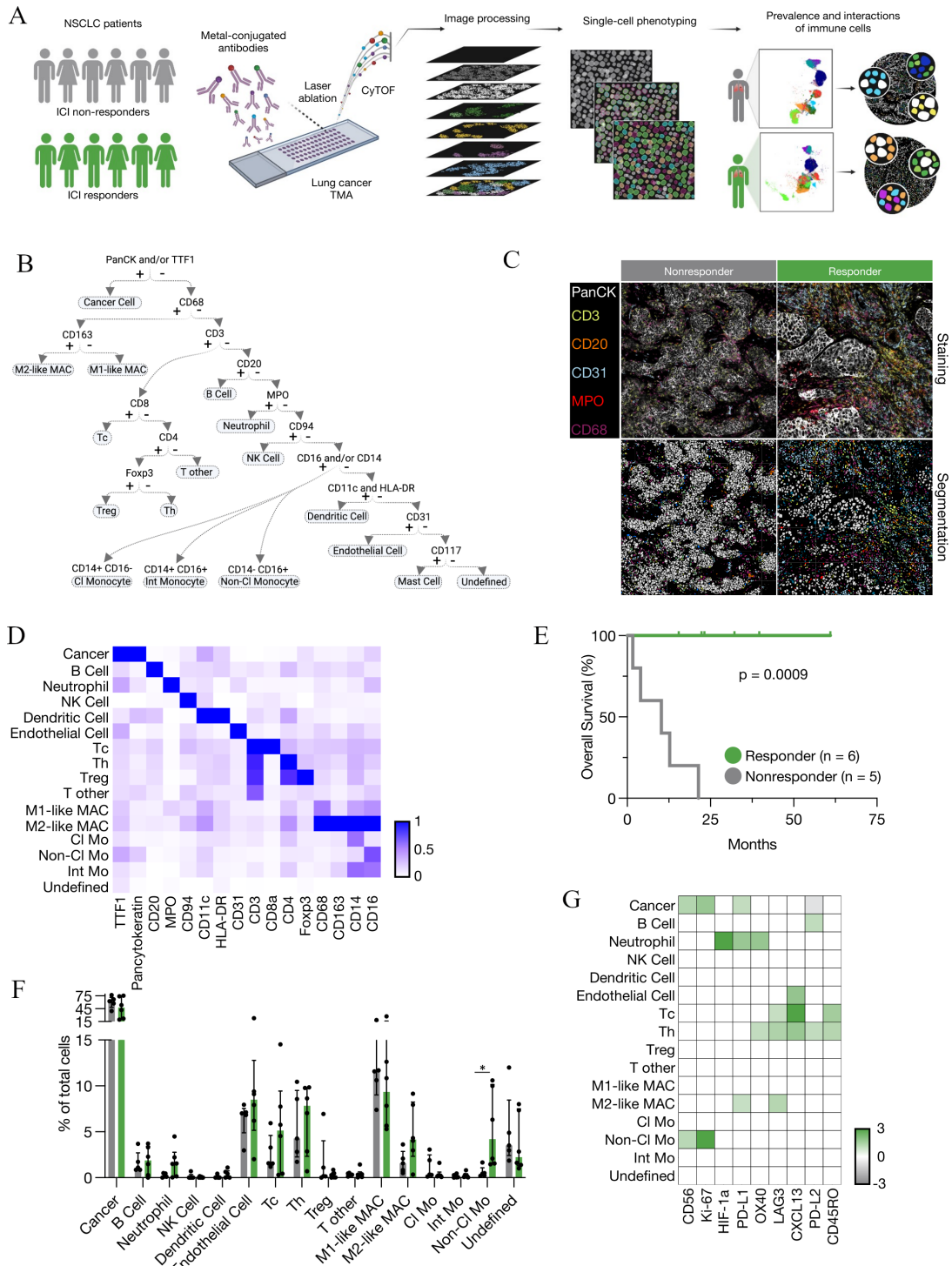


Figure 1 Single cell spatial landscape of response to ICI in NSCLC. (A) Schematic of IMC acquisition of multiplexed images from 27 patients with NSCLC, involving laser ablation of metal-conjugated antibodies, CyTOF acquisition, single-cell phenotyping and characterization of the prevalence and interactions of immune cells. (B) Cell assignment hierarchy. (C) Representative images of antibody staining and corresponding single-cell segmented images for responders and non-responders. (D) Average expression of markers in indicated cell populations. (E) Kaplan-Meier overall survival analysis for 11 patients with NSCLC treated with ICI (responders n=6, non-responders n=5). (F) Frequency of cancer and immune cell populations in responders and non-responders to immune checkpoint inhibitors as a proportion of total cells. Non-CI Mo - responders versus non-responders: *p=0.017316. (G) Ratio of average marker intensity in cancer and immune cell populations. Green represents higher intensity in responders, gray in non-responders and white was not calculated. Median±IQR. Statistical analysis (E: log-rank test, F: Mann-Whitney test). CI Mo, classical monocyte; CyTOF, cytometry by time of flight; DC, dendritic cell; ICI, immune checkpoint inhibitor; IMC, imaging mass cytometry; Int Mo, intermediate monocyte; M1-like MAC, M1-like macrophage; M2-like MAC, M2-like macrophage; NK cell, natural killer cell; Non-CI Mo, non-classical monocyte; NSCLC, non-small cell lung cancer; Tc, cytotoxic T cell; Th, helper T cell; TMA, tissue microarray; Treg, regulatory T cell.

Steps were performed in line with the Ventana discovery ULTRA staining module (Roche Diagnostic). Briefly, deparaffinization was followed by cell conditioning using conditioner #1 at 95°C for 56 min and primary antibody incubation for 60 min. Then, one Drop of Omap anti-RB HRP (Roche Diagnostic) was applied with a 16 min incubation followed by incubation with one drop of hematoxylin (Roche Diagnostic) for 16 min. Finally, one drop of bluing reagent (Roche Diagnostic) was used for 4 min.

Spectral flow cytometry

Tumors were isolated, mechanically dissociated and filtered through a 40 µm mesh. Red blood cell lysis was performed with BD Pharm Lyse buffer (BD Biosciences). Samples were enriched for leukocytes using Percoll centrifugation, pH 8.5–9.5 (25°C) (Sigma-Aldrich). Dead cell exclusion was performed with LIVE/DEAD Aqua (Thermo Fisher Scientific) as per manufacturer instructions. Samples were incubated with Fc block for 20 min (1:100; BD Biosciences), followed by incubation with antibodies (30 min, online supplemental table 4 including marker, color, dilution, clone and supplier). Cytex Aurora (SpectroFlo) was used for spectral flow cytometry. OneComp eBeads (eBioscience) and/or tumor cells were used for compensation controls. Dead cells and debris were excluded from analyses using forward scatter × side scatter and LIVE/DEAD stain. Mouse immune populations were defined as seen in online supplemental figure 5; CD8 antigen experienced T cells were gated as previously described.²⁴ FlowJo V.10.8.0 (BD) was used for analysis. Tumors with significant ulceration were excluded from analysis.

For the Uniform Manifold Approximation and Projection (UMAP), the DownSample and UMAP FlowJo plugins were used. Briefly, samples that had more than 5000 live CD45+ cells were included. Individual samples were downsampled on the CD45+ live population to yield the same number of cells per treatment group in each trial for a total of 34,880 cells per treatment group. All samples were concatenated and the UMAP plugin was run on the CD45+ live cells using the Euclidean setting with 15 nearest neighbors, 0.5 minimum distance, 0.2 number of components and the compensated parameters were included. B cells, monocytes, Ly6C⁻ Ly6G⁻ CD11b+ cells, Tregs, dendritic cells, CD4+ T cells, neutrophils, CD8+ T cells, and other cells were gated on the concatenated sample as shown in online supplemental figure 5. The same procedure was repeated to run a UMAP on T cells for all samples that had more than 2000 T cells. Antigen experienced CD8+ and CD4+ T cells were gated on the concatenated sample as shown in online supplemental figure 5.

Statistical analysis and workflow

Statistical analyses were performed using GraphPad Prism V.9 statistical software. All image analysis steps were performed in Python (V.3.7.12) and MATLAB (V.2019b). Data were expressed as mean ± SEM or median ± IQR; p

values < 0.05 were considered significant (or as indicated). Log-rank (Mantel-Cox) test was used for survival analyses.

RESULTS

To characterize the immune microenvironment underlying ICI response, we performed IMC on surgically resected samples from 27 patients with NSCLC (figure 1a–d, online supplemental tables 1,2). Our optimized panel included 35 antibodies targeting 14 cell lineage markers, 11 co-stimulatory/inhibitory markers, 6 immune signaling markers and four tissue structural markers, allowing us to define up to 15 cellular lineages with functionally diverse identities (online supplemental figure S1a,b, online supplemental table 3). Images were segmented into individual cells using a combination of classical and modern machine learning-based computer vision algorithms²⁵ (online supplemental figure 1C). This fully automated approach eliminates bias and enables high-throughput segmentation across a variety of diverse tissue types. Using this approach, we detected 114,524 spatially-resolved cells within the tumor niche. A supervised hierarchical lineage assignment approach was then used to classify each cell based on canonical lineage markers for major immune populations, tumor cells or blood vessels (figure 1B).

As the TIME at different anatomical locations is known to regulate tumor growth, metastasis, and therapeutic responses,²⁶ patients were first separated based on the location of tumor resection (lung vs metastases). Eleven patients in our cohort had tumors resected from the lung; six responders and five non-responders (figure 1e), and the single-cell spatial landscape of the tumor immune contexture was compared. We first assessed the frequency of immune populations between responders and non-responders. The most significantly elevated immune population in responders compared with non-responders was CD14⁻ CD16⁺ non-classical monocytes (figure 1f), which are known for their ability to patrol the vasculature in a steady state. However, studies have shown that non-classical monocytes are not restricted to tissue-repair responses and can exhibit context-dependant inflammatory features which may include T-cell activation and inflammatory cytokine production.^{27–28} Therefore, we explored the functional status of adaptive immune cells by comparing the mean expression intensity of functional markers across immune subsets between responders and non-responders (figure 1g, online supplemental figure 2a–b). As expected, responders expressed higher levels of PD-L1 on cancer cells and increased expression of CD45RO on T cells, a marker for memory T cells that correlates with ICI response (figure 1g).²⁹ In responders, we also observed elevated expression of LAG3 on CD8+ T cells (figure 1g).³⁰ Of note, one of the most upregulated markers on CD8+ T cells in responders was CXCL13 (figure 1g), an emerging biomarker for immunotherapy efficacy.³¹ CD8+ T cells expressing high levels of PD-1 have been shown to constitutively express CXCL13 in

the context of NSCLC, permitting immune cell recruitment to tertiary lymphoid structures and mediating an improved response to PD-1 blockade.³²

To determine the frequency of activated cell types beyond their intensity of expression, we compared the prevalence of activated cell types between responders and non-responders. We observed a significantly greater prevalence of PD-L1+ cancer cells, LAG3+CD4+ T helper cells and increased LAG3+Ki-67⁺ T cells in responders compared with non-responders highlighting the association between increased T-cell exhaustion and response to ICI (online supplemental figure 2c-e). With recent high profile studies establishing a strong link between CXCL13 expression and immunotherapy efficacy,^{31,33} we next further examined the relationship between CXCL13 expressing cells and response to ICI in our dataset. Consistent with prior reports, we found significantly more CXCL13+ T cells in responders compared with non-responders (figure 2A, online supplemental figure 2f-h). Interestingly, we found that 63% of the cells expressing CXCL13 were not T cells, but rather endothelial cells, macrophages, monocytes, B cells and cancer cells (figure 2B), indicating that this important ligand has multiple cellular sources within the tumor niche.

To interrogate spatially nuanced cell–cell interactions between components of the TIME, we employed a permutation tests strategy to quantify the likelihood of pairwise interaction or avoidance between cells from distinct lineages (figure 2C).⁷ Tumor cells had almost exclusive homotypic (tumor–tumor) interactions in both responders and non-responders. B cells had a stronger tendency to interact with CD8+ cytotoxic T cells, CD4+ helper T cells and MHCII+ dendritic cells in responders (figure 2C)—all crucial cell types in the formation of tertiary lymphoid structures (TLS). Although we did not see distinct TLS within our 1 mm² cores, these structures are found within or proximal to tumors, allow for local presentation of antigen and maintain T cell-mediated antitumor responses.^{34,35} They have been associated with improved prognosis across several malignancies and their density has been correlated with improved response to ICI in melanoma, sarcoma, and a cohort of solid tumors irrespective of CD8+ T cell density and PD-L1 status.^{36–39} Non-classical monocytes, which we discovered were enriched in responders (figure 1F), were more likely to interact with T cells from responders compared with non-responders (figure 2C), consistent with the notion that they may influence the functional status of T cells.^{27,28} Interestingly, macrophages, regardless of the polarization state, had a higher tendency for interaction with most cell types in the TIME of responders, suggestive of a global active macrophage population with ICI response.

To further elucidate the spatially-resolved TIME landscape of ICI response, we created cellular neighborhoods where we identified the 10 nearest spatial neighbors for each individual cell. Then, we reclassified each cell based on their spatially defined cellular neighborhood (CN).²² Using this approach, we discovered seven CNs

that recapitulated both novel and known tissue architectures, which we named: tumor stroma, vascular niche, pan-immune-1 and pan-immune-2, tumor core, lymphoid-enriched, and monocyte-enriched neighborhoods (figure 2D). Interestingly, despite identifying no differences in the number of endothelial cells between responders and non-responders (figure 1F), we found that the vascular niche CN was significantly enriched in responders (figure 2E). The close proximity between endothelial cells and both B and T lymphocytes which demarcates this CN, may indicate an enrichment of high endothelial venules in the responder cohort. These specialized endothelial cells are required for the maintenance of immune responses by contributing to lymphocyte migration and have been associated with improved response to ICIs in patients with metastatic melanoma.^{40,41} Interestingly, within the vascular niche (CN2), CXCL13+ endothelial cells were exclusively found in responders (three out of six patients; compared with zero out of five non-responder patients, online supplemental figure 2i). This trend suggested that beyond T cells, the expression of CXCL13 by other cell types in the TIME may also be associated with response.

We next assessed the composition of patient samples from metastases (eight responders and eight non-responders, online supplemental table 2, online supplemental figure 3a). In contrast to tumors resected from the lung, we found no significant associations between response to ICI and prevalence of cancer, immune or endothelial cell types (online supplemental figure 3b). Moreover, we found no association between prevalence of CXCL13+ T cells and response to ICI, including for both CD4+ and CD8+ subsets (online supplemental figure 3c). These findings highlight that tissue-specific features of the TIME may have a profound impact on therapeutic response and that elucidating these features is important to develop effective biomarkers of immunotherapy efficacy.

Given that CXCL13 expression as a biomarker of response to ICIs has been established,^{31,33} and our finding of enhanced CXCL13+ T cells in responders versus non-responders (figures 1G and 2A), we next tested the functional relevance of CXCL13 in immunotherapy efficacy. As multiple cell types were found to express CXCL13 in the TIME (figure 2B), we reasoned that treating tumors with rCXCL13 may lend insight into its putative ability to potentiate anti-PD-1 efficacy as a combination therapy. Using syngeneic mouse models of cancer, we combined anti-PD-1 with peritumoral injection rCXCL13, to mimic its high levels within the tumor niche of ICI responders agnostic of its cellular source (see figure 3A for trial schematic). We selected models that recapitulated key TIME archetypes including (1) ‘immune-infiltrated, ICI sensitive’, where CD8+ T cells are abundant and functional within tumors that display sensitivity to ICI (HKP1 lung cancer cells^{38,39}; figure 3B,C); (2) ‘immune-infiltrated, ICI resistant’, where CD8+ T cells are also abundant but remain dysfunctional, so tumors are resistant to ICI

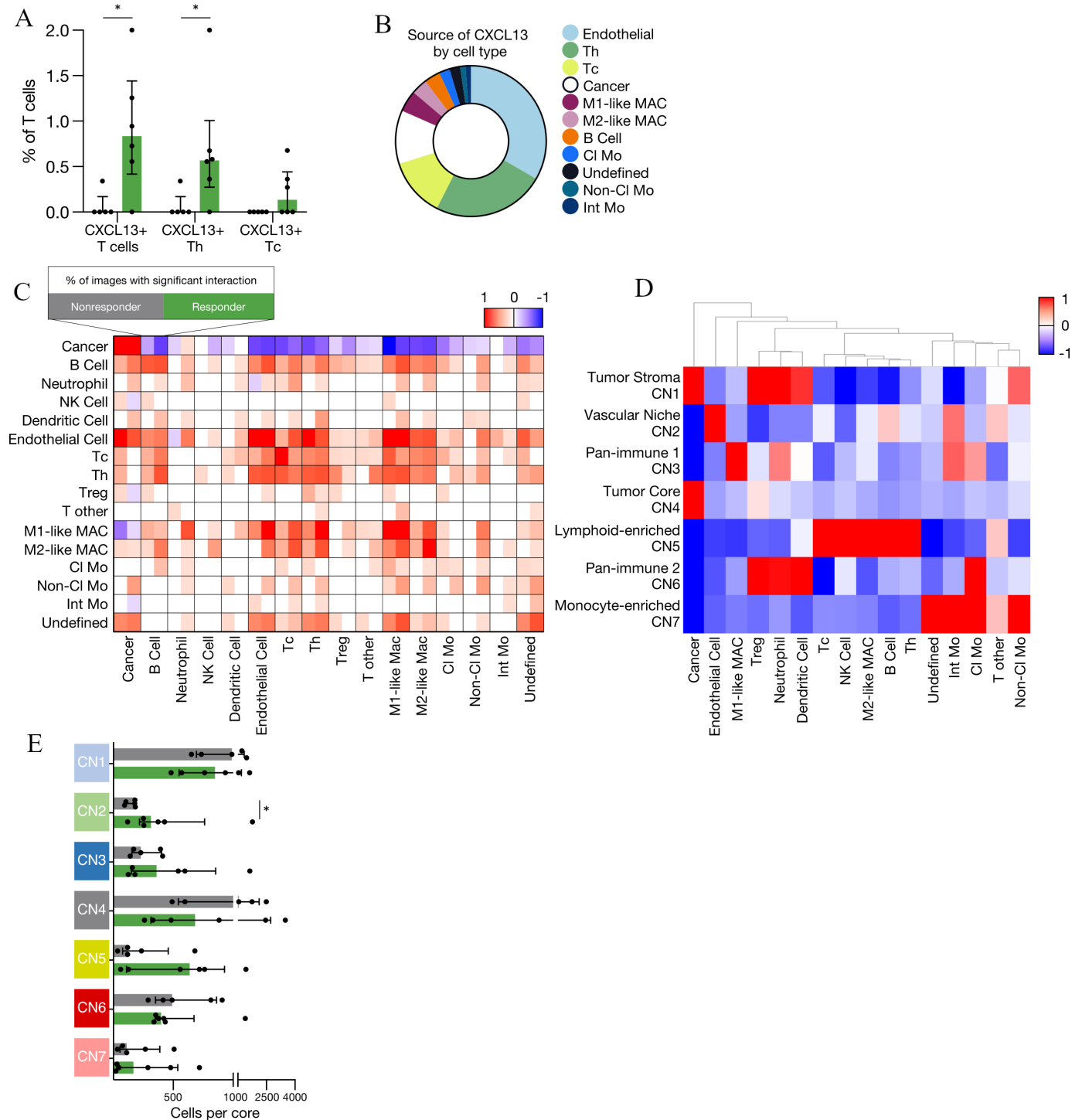


Figure 2 Cell-cell communication and spatial neighborhoods associated with response to ICI in NSCLC. (A) Prevalence of CXCL13+ T cells, CXCL13+ Th and CXCL13+ Tc across non-responders and responders as a proportion of T cells. CXCL13+ T cells – non-responders versus responders: $*p=0.021645$. CXCL13+ Th non-responders versus responders: $*p=0.021645$. (B) Pie chart indicating the relative proportion of cell types expressing CXCL13 ($n=11$). (C) Heatmap indicating significant pairwise cell-type interaction (red) or avoidance (blue) summarized across the two-sided permutation tests on individual images ($n=11$ images; 1000 permutations each). (D) Heatmap of seven cellular neighborhoods discovered in 11 patients with NSCLC. (E) Number of cells per cellular neighborhood in non-responders and responders to ICI (CN2 – non-responders vs responders $*p=0.0303$). Median \pm IQR. Statistical analysis (A, E: Mann-Whitney test). Cl Mo, classical monocyte; ICI, immune checkpoint inhibitor; Int Mo, intermediate monocyte; M1-like MAC, M1-like macrophage; M2-like MAC, M2-like macrophage; NK cell, natural killer cell; NSCLC, non-small cell lung cancer; Tc, cytotoxic T cell; Th, helper T cell; Treg, regulatory T cell.

(MC38 colorectal cancer cells²³; [figure 3D,E](#)); and (3) ‘immune desert’ (also known as ‘immune cold’), with few or no detectable CD8+ T cells rendering these tumors also resistant to ICI (LLC1 lung cancer cells; [figure 3F,G](#)).^{5 42} Interestingly, across models, we observed differences in the ability of rCXCL13 to potentiate anti-PD-1 efficacy. In HKP1 ‘infiltrated-sensitive’ tumors, treatment with anti-PD-1 alone significantly decreased tumor volume compared with IgG control, as expected; however, the addition of peritumoral rCXCL13 further potentiated anti-PD-1 response ([figure 3B,C](#), online supplemental figure 4a). Remarkably, peritumoral administration of rCXCL13 was able to induce anti-PD-1 response even in MC38 ‘infiltrated-resistant’ tumors that were insensitive to anti-PD-1 therapy alone ([figure 3D,E](#), online supplemental figure 4b). This finding was confirmed in a second ‘infiltrated-resistant’ model of B16–F10 melanoma, where treatment with rCXCL13 was sufficient to sensitize tumors to anti-PD-1 (online supplemental figure 4c-d). Finally, in LLC1 ‘desert-resistant’ tumors that are largely devoid of infiltrating T cells, we observed no effect of anti-PD-1 on tumor volume, nor was rCXCL13 able to improve efficacy ([figure 3F,G](#), online supplemental figure 4e). These data demonstrate the ability of CXCL13 to enhance the sensitivity of tumors to anti-PD-1 as long as they are sufficiently immune-infiltrated.

To characterize the immune changes associated with rCXCL13 and anti-PD-1 combination therapy, we performed spectral flow cytometry on tumor tissues using a 22-plex antibody panel to define 21 functionally distinct immune populations (online supplemental figure 5, online supplemental table 4). Key differences were observed in immune frequencies between models ([figure 4A–C](#)). As expected, HKP1 and MC38 immune-infiltrated tumors had high frequencies of CD8+ T cells compared with LLC1 immune-desert tumors ([figure 4A–C](#), online supplemental figures 6–8). Echoing our IMC findings in patients ([figure 1F](#)), we also found that monocytes were associated with ICI response in our mouse models. Particularly, when comparing treatment-control experimental groups (IgG and PBS), CCR2⁺ monocytes (resembling non-classical monocytes in humans^{14 43}) were enriched in HKP1 ICI-sensitive tumors, whereas CCR2⁺ monocytes (resembling classical monocytes) were the dominant subset in MC38 and LLC1 ICI-resistant tumors ([figure 4D](#), online supplemental figures 6–8). Consistently, when rCXCL13 was combined with anti-PD-1, we observed an enrichment in the CCR2⁺ monocyte fraction in all models ([figure 4E–G](#)). [figure 3C,E](#)[figure 3G](#) Although non-classical monocytes are typically restricted to the blood vessels in steady state, they are found within tumors in mice and humans.¹⁴ Similarly, classical monocytes are known for their pro-inflammatory functions; however, paradoxically, they can adopt potent immunosuppressive roles in the TIME.⁴⁴ Reinforcing the existence of unique monocyte functional states in cancer, our data reinforce a putative role for the balance of monocyte subsets in the context of immunotherapy, and suggest

that targeting specific monocyte subsets may augment ICI response.⁴⁴

We next quantified differences in the functional status of T cells across models and treatment groups as a reflection of ICI efficacy. In HKP1 ‘infiltrated-sensitive’ tumors, despite no significant increase in total CD8+ or CD4+ T cells when rCXCL13 was combined with anti-PD-1, we found an enrichment in CD11a+CD49d+ antigen-experienced CD4+ T cells in response to combination therapy where efficacy was highest ([figure 4H](#), online supplemental figure 6). We also discovered a significant increase in MHCII+ dendritic cells within these tumors, which are critical regulators of adaptive immunity and ICI efficacy in cancer ([figure 4I](#), online supplemental figure 6).⁴⁵ Interestingly, in the MC38 ‘infiltrated-resistant’ model, combining rCXCL13 with anti-PD-1 similarly increased CD11a^{hi} antigen-experienced CD8+ T cells ([figure 4J](#)). However, we concurrently observed an increase in total CD8+ T-cell frequencies ([figure 4K](#), online supplemental figure 7), potentially underlying the ability of rCXCL13 to induce ICI sensitivity in this model (in contrast to HKP1 tumors, which are sensitive to ICI from the outset and therefore may not need this additional boost). Consistent with this notion, we saw minimal changes in the T-cell compartment in LLC1 ‘desert-resistant’ tumors ([figure 4L,M](#), online supplemental figure 8), aligning with their inability to respond to any of the treatment groups. These data provide functional evidence that rCXCL13 can enhance T-cell function to improve ICI efficacy in immune-infiltrated tumors, even in cases of inherent resistance to PD-1 blockade.

DISCUSSION

Spatial single-cell technologies enable the visualization of a substantial number of cell lineages, functional states and coordinated cellular neighborhoods within the tumor niche.⁴⁶ In breast,^{7 12 47 48} colorectal,⁴⁹ and pancreatic cancer,¹¹ these approaches have led to the discovery of novel features of the tumor microenvironment that are associated with clinical outcomes.^{7 49} Here, we report one of the first single-cell spatially-resolved dissections of ICI efficacy in lung cancer. Using imaging mass cytometry, we visualized 114,524 cells within the tumor niche of 27 patients with lung cancer treated with ICI. This analysis identified non-classical monocytes, distinct T-cell interactions, and CXCL13 as critical mediators of ICI response. Importantly, using murine models of lung, melanoma and colorectal cancer, we demonstrate that CXCL13 functionally contributes to ICI efficacy and provide mechanical insights that parallels what we observe in human correlative studies.

Remarkably, despite the large time frame for some patients between sample collection and treatment with ICI, we observed elevated levels of canonical biomarkers of response to ICI in our responder cohort. Namely, we observed higher PD-L1 expression on cancer cells, with elevated LAG3 and CXCL13 expressing T cells.

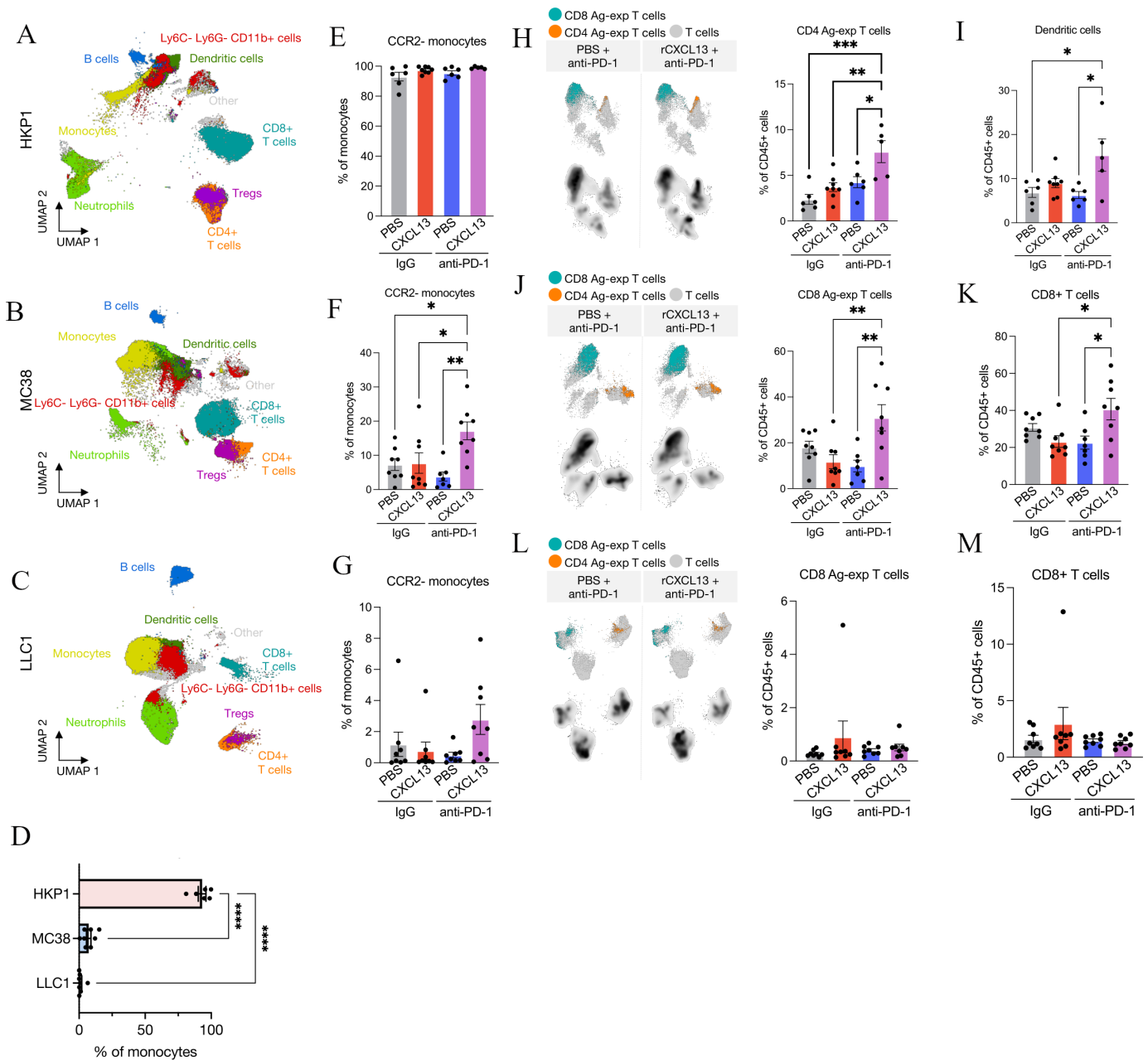


Figure 4 The rCXCL13 and anti-PD-1 lead to recruitment of antigen-experienced T cells. Uniform Manifold Approximation and Projection (UMAP) of total CD45⁺ cells from combining all treatment groups in (A) HKP1, (B) MC38 or (C) LLC1 models. (D) Average frequency of CCR2⁻ monocytes in IgG+ PBS control tumors. Average frequency of CCR2⁻ monocytes in (E) HKP1, (F) MC38, (G) LLC1. UMAP plot of all T cells highlighting antigen-experienced CD4⁺ and CD8⁺ T-cell abundance in (H) HKP1, (J) MC38 or (L) LLC1 models with indicated treatments. Average frequency of dendritic cells in (I) HKP1 or CD8⁺ T cells in (K) MC38 and (M) LLC1 models. Mean ± SEM. Statistical analysis (D–M: one-way analysis of variance with Tukey multiple comparisons test). PBS, phosphate-buffered saline; PD-1, programmed cell death protein-1; rCXCL13, recombinant CXCL13; Tregs, regulatory T cells.

This suggests that there may be an immunological and microenvironmental ‘memory’ within lung tumors that preserves a coordinated immune response over time.

CXCL13 is a canonical regulator of B-cell recruitment and organization within lymphoid organs, and can orchestrate the formation of tertiary lymphoid structures.^{50 51} Recently, the role of this chemokine has gained significant interest in the context of response to immune checkpoint blockade across multiple tumor types. A pan-cancer

meta-analysis of 1000 patients with ICI-treated cancer determined that out of all genes upregulated in CD8⁺ tumor infiltrating lymphocytes positive for a clonal neoantigen multimer, *CXCL13* was the most upregulated in ICI responders compared with non-responders.³¹ Moreover, using a patient-derived tumor fragment platform, high CXCL13 protein levels were found to be predictive of ICI efficacy to the same extent as the presence of PD-1 high T cells.³³ In NSCLC, CD4⁺ T cells expressing PD-1 and

CXCL13 were found to interact with antigen-presenting cells in the tumor microenvironment to mediate the anti-tumor effects of anti-PD-1 therapy.⁵² These studies shed important light on the role of CXCL13-expressing T cells in shaping ICI response, but the effects of CXCL13 as an effector molecule itself remain poorly understood. Indeed, in our data set, 63% of the CXCL13 producing cells are not T cells. Given the canonical role of CXCL13 as a secreted chemokine, we demonstrate that rCXCL13, agnostic of cellular source, potentiates the effects of anti-PD-1 across ICI-sensitive and ICI-resistant models, and highlights how CXCL13 is an important mediator of immunotherapy efficacy, beyond serving as a correlative biomarker.^{31 33}

Through our *in vivo* functional analyses, we discovered that soluble CXCL13 exerts its effects in the tumor immune microenvironment through its impact on two distinct immune cell populations. First, rCXCL13 increases the prevalence of antigen-experienced CD8⁺ and CD4⁺ T cells, which are then re-invigorated by the addition of anti-PD-1. Second, the combination of rCXCL13 and anti-PD-1 reduces the levels of CCR2⁺ monocytes relative to CCR2⁻ monocytes in the tumor microenvironment in association with improved ICI efficacy. This aligns with our imaging mass cytometry discoveries in patient samples, where we observed an increase in non-classical monocytes in ICI responders versus non-responders. Monocytes expressing CCR2 can become highly immunosuppressive in the tumor microenvironment⁵³ and the combination of CCR2 antagonists and anti-PD-1 inhibitors have shown synergism in terms of reducing tumor volume in preclinical models.^{54 55} Blockade of CCR2 has also been associated with an increased influx of CD8⁺ T cells into subcutaneous tumors.⁵⁴ Therefore, these findings suggest CXCL13 may elicit its effects in part by disarming immunosuppressive monocyte signals.

A limitation of our study includes the small sample size, which is not representative of the prevalence of ICI response in patients with NSCLC. Additionally, a 1 mm core per patient does not capture the well-known tumor heterogeneity that might exist within a primary lesion, nor does it capture features of tumor evolution throughout the patient trajectory of recurrence and progression over time. However, such tissue cores are highly representative of what may be captured by a routine clinical core needle biopsy—the mainstay of diagnosis and biomarker analysis that currently inform the entire therapeutic strategy offered to the vast majority of patients with locally advanced or metastatic NSCLC.

Overall, our multidimensional interrogation of ICI response in NSCLC highlights the complexity of TIME features that robustly associate with ICI efficacy. Future studies on how spatial and phenotypic TIME cellular relationships influence treatment outcomes are warranted and may lead to more accurate biomarkers of response. From a practical perspective, while we recognize the limited clinical applications of rCXCL13 as an intervention strategy, we demonstrate that CXCL13 is

mechanistically active as a soluble effector molecule within the tumor microenvironment and is able to potentiate anti-PD-1 therapy. Future studies should focus on targeting the pathways involved in the repression of CXCL13 production by immune cells, or on enhancing CXCL13-mediated cellular interactions.

Author affiliations

¹Rosalind and Morris Goodman Cancer Institute, McGill University, Montreal, Quebec, Canada

²Department of Human Genetics, McGill University, Montreal, Quebec, Canada

³Department of Psychology and Computer Science, University of Toronto, Toronto, Ontario, Canada

⁴Department of Physiology, McGill University, Montreal, Quebec, Canada

⁵Institut Universitaire de Cardiologie et de Pneumologie de Québec, Université Laval, Québec City, Quebec, Canada

⁶Department of Medicine, Division of Experimental Medicine, McGill University, Montreal, Quebec, Canada

⁷Department of Surgery, McGill University, Montreal, Quebec, Canada

Twitter Mark Sorin @sorin_mark, Morteza Rezanejad @mo_rezanejad, Miranda W Yu @Miranda_WYu, Lysanne Desharnais @LysDesharnais, Sheri A C McDowell @mcdowell_sheri, Samuel Doré @SamuelDore9, Roni Rayes @ronirayes, Daniela F Quail @DanielaQuail, Philippe Joubert @PJoubertPatho, Jonathan D Spicer @DoctorJSpicer and Logan A Walsh @loganawalsh

Acknowledgements The authors are grateful for support from the Single Cell Imaging and Mass Cytometry Analysis Platform (SCIMAP), the Histology Core (N. Robinson and P. Cruz), and the Flow Cytometry facility (C. Stegen and J. Leconte) at the Rosalind and Morris Goodman Cancer Institute, as well as support from the Quebec Cancer Consortium and the financial support from the Ministère de l'Économie et de l'Innovation du Québec through the Fonds d'accélération des collaborations en santé. Tissues were obtained through the Quebec Respiratory Health Research Network-IUCPQ site Biobank.

Contributors MS, JDS, and LAW designed the study, reviewed the data, and wrote the manuscript. MS, EK, and MR oversaw and performed all experiments and data analysis. DFQ provided essential insight throughout the study and wrote the manuscript. BF provided bioinformatics support. MY, LD, SM, SD, AA, VB, YW, and RR provided experimental support and/or optimized protocols. MO, FC, VM, AG, and PJ provided human tissue samples, built the patient tissue microarray and collected and curated all clinical data. LAW is responsible for the overall content.

Funding This study was funded by the Canada Foundation for Innovation (LAW JELF-39178), Canadian Institutes of Health Research (LAW PJT-162137) and The Brain Tumor Funders' Collaborative (LAW and DFQ). LAW is supported by a Rosalind and Morris Goodman Chair in Lung Cancer Research. MS is supported by a Fonds de recherche du Québec - Santé Doctoral award, the Hilton J. McKeown Scholarship and the Vanier Canada Graduate Scholarship. JDS is supported by the Fonds de recherche du Québec - Santé Clinician Scientist Junior 2 award and by the Montreal General Hospital Foundation Dr Ray Chiu Distinguished Scientist in Surgical Research Award.

Competing interests None declared.

Patient consent for publication Not applicable.

Ethics approval The protocol for human sample biobanking was approved (ethics, scientific and final) by the Institut Universitaire de Cardiologie et de Pneumologie de Québec, Protocol Number: IRB # 2022-3674, 22090. Participants gave informed consent to participate in the study before taking part.

Provenance and peer review Not commissioned; externally peer reviewed.

Data availability statement Data are available upon reasonable request.

Supplemental material This content has been supplied by the author(s). It has not been vetted by BMJ Publishing Group Limited (BMJ) and may not have been peer-reviewed. Any opinions or recommendations discussed are solely those of the author(s) and are not endorsed by BMJ. BMJ disclaims all liability and responsibility arising from any reliance placed on the content. Where the content includes any translated material, BMJ does not warrant the accuracy and reliability of the translations (including but not limited to local regulations, clinical guidelines, terminology, drug names and drug dosages), and is not responsible for any error and/or omissions arising from translation and adaptation or otherwise.

Open access This is an open access article distributed in accordance with the Creative Commons Attribution Non Commercial (CC BY-NC 4.0) license, which permits others to distribute, remix, adapt, build upon this work non-commercially, and license their derivative works on different terms, provided the original work is properly cited, appropriate credit is given, any changes made indicated, and the use is non-commercial. See <http://creativecommons.org/licenses/by-nc/4.0/>.

ORCID iDs

Benoit Fiset <http://orcid.org/0000-0003-0372-8868>

Logan A Walsh <http://orcid.org/0000-0001-8771-2577>

REFERENCES

- Haslam A, Prasad V. Estimation of the percentage of US patients with cancer who are eligible for and respond to checkpoint inhibitor immunotherapy drugs. *JAMA Netw Open* 2019;2:e192535.
- Ribas A, Wolchok JD. Cancer immunotherapy using checkpoint blockade. *Science* 2018;359:1350–5.
- Bai R, Chen N, Li L, et al. Mechanisms of cancer resistance to immunotherapy. *Front Oncol* 2020;10.
- Boyero L, Sánchez-Gastaldo A, Alonso M, et al. Primary and acquired resistance to immunotherapy in lung cancer: unveiling the mechanisms underlying of immune checkpoint blockade therapy. *Cancers* 2020;12. doi:10.3390/cancers12123729. [Epub ahead of print: 11 12 2020].
- Chen DS, Mellman I. Elements of cancer immunity and the cancer-immune set point. *Nature* 2017;541:321–30.
- Galon J, Bruni D. Approaches to treat immune hot, altered and cold tumours with combination immunotherapies. *Nat Rev Drug Discov* 2019;18:197–218.
- Jackson HW, Fischer JR, Zanutelli VRT, et al. The single-cell pathology landscape of breast cancer. *Nature* 2020;578:615–20.
- Keren L, Bosse M, Marquez D, et al. A structured Tumor-Immune microenvironment in triple negative breast cancer revealed by multiplexed ion beam imaging. *Cell* 2018;174:1373–87.
- Ali HR, Jackson HW, Zanutelli VRT, et al. Imaging mass cytometry and multiplatform genomics define the phenogenomic landscape of breast cancer. *Nat Cancer* 2020;1:163–75.
- Schürch CM, Bhate SS, Barlow GL, et al. Coordinated cellular neighborhoods orchestrate antitumoral immunity at the colorectal cancer invasive front. *Cell* 2020;182:1341–59.
- Liudahl SM, Betts CB, Sivagnanam S, et al. Leukocyte heterogeneity in pancreatic ductal adenocarcinoma: phenotypic and spatial features associated with clinical outcome. *Cancer Discov* 2021;11:2014–31.
- Carvajal-Hausdorf DE, Patsenker J, Stanton KP, et al. Multiplexed (18-Plex) measurement of signaling targets and cytotoxic T cells in trastuzumab-treated patients using imaging mass cytometry. *Clin Cancer Res* 2019;25:3054–62.
- Moldoveanu D, Ramsay L, Lajoie M, et al. Spatially mapping the immune landscape of melanoma using imaging mass cytometry. *Sci Immunol* 2022;7:eabi5072.
- Zilionis R, Engblom C, Pfirschke C, et al. Single-cell transcriptomics of human and mouse lung cancers reveals conserved myeloid populations across individuals and species. *Immunity* 2019;50:1317–34.
- Liu B, Hu X, Feng K, et al. Temporal single-cell tracing reveals clonal revival and expansion of precursor exhausted T cells during anti-PD-1 therapy in lung cancer. *Nat Cancer* 2022;3:108–21.
- Yang Q, Zhang H, Wei T, et al. Single-cell RNA sequencing reveals the heterogeneity of tumor-associated macrophage in non-small cell lung cancer and differences between sexes. *Front Immunol* 2021;12:756722.
- Leader AM, Grout JA, Maier BB, et al. Single-cell analysis of human non-small cell lung cancer lesions refines tumor classification and patient stratification. *Cancer Cell* 2021;39:1594–609.
- McDowell SAC, Luo RBE, Arabzadeh A, et al. Neutrophil oxidative stress mediates obesity-associated vascular dysfunction and metastatic transmigration. *Nat Cancer* 2021;2:545–62.
- Vassilvitskii S, Arthur D. In proceedings of the eighteenth annual ACM-SIAM Symposium on discrete algorithms:1027–35.
- Peel D, MacLahlan G. *Finite mixture models*. John & Sons, 2000.
- Schapiro D, Jackson HW, Raghuraman S, et al. histoCAT: analysis of cell phenotypes and interactions in multiplex image cytometry data. *Nat Methods* 2017;14:873–6.
- Schürch CM, Bhate SS, Barlow GL, et al. Coordinated cellular neighborhoods orchestrate antitumoral immunity at the colorectal cancer invasive front. *Cell* 2020;183:838.
- Arabzadeh A, Chan C, Nouvion A-L, et al. Host-related carcinoembryonic antigen cell adhesion molecule 1 promotes metastasis of colorectal cancer. *Oncogene* 2013;32:849–60.
- Liu X, Gibbons RM, Harrington SM, et al. Endogenous tumor-reactive CD8⁺ T cells are differentiated effector cells expressing high levels of CD11a and PD-1 but are unable to control tumor growth. *Oncoimmunology* 2013;2:e23972.
- Elham Karimi MR, Fiset B, Perus L. Machine learning meets classical computer vision for accurate cell identification. *bioRxiv* 2022.
- Oliver AJ, Lau PKH, Unsworth AS, et al. Tissue-dependent tumor microenvironments and their impact on immunotherapy responses. *Front Immunol* 2018;9:70.
- Westhorpe CLV, Norman MU, Hall P, et al. Effector CD4⁺ T cells recognize intravascular antigen presented by patrolling monocytes. *Nat Commun* 2018;9:747.
- Bianchini M, Duchêne J, Santovito D, et al. PD-L1 expression on nonclassical monocytes reveals their origin and immunoregulatory function. *Sci Immunol* 2019;4. doi:10.1126/sciimmunol.aar3054. [Epub ahead of print: 21 Jun 2019].
- Tietze JK, Angelova D, Heppt MV, et al. The proportion of circulating CD45RO⁺CD8⁺ memory T cells is correlated with clinical response in melanoma patients treated with ipilimumab. *Eur J Cancer* 2017;75:268–79.
- Gramaglia I, Jember A, Pippig SD, et al. The OX40 costimulatory receptor determines the development of CD4 memory by regulating primary clonal expansion. *J Immunol* 2000;165:3043–50.
- Litchfield K, Reading JL, Puttick C, et al. Meta-analysis of tumor- and T cell-intrinsic mechanisms of sensitization to checkpoint inhibition. *Cell* 2021;184:596–614.
- Thommen DS, Koelzer VH, Herzig P, et al. A transcriptionally and functionally distinct PD-1⁺ CD8⁺ T cell pool with predictive potential in non-small-cell lung cancer treated with PD-1 blockade. *Nat Med* 2018;24:994–1004.
- Voabil P, de Bruijn M, Roelofs LM, et al. An ex vivo tumor fragment platform to dissect response to PD-1 blockade in cancer. *Nat Med* 2021;27:1250–61.
- Sautès-Fridman C, Petitprez F, Calderaro J, et al. Tertiary lymphoid structures in the era of cancer immunotherapy. *Nat Rev Cancer* 2019;19:307–25.
- Trüb M, Zippelius A. Tertiary lymphoid structures as a predictive biomarker of response to cancer immunotherapies. *Front Immunol* 2021;12:674565.
- Petitprez F, de Reyniès A, Keung EZ, et al. B cells are associated with survival and immunotherapy response in sarcoma. *Nature* 2020;577:556–60.
- Helmink BA, Reddy SM, Gao J, et al. B cells and tertiary lymphoid structures promote immunotherapy response. *Nature* 2020;577:549–55.
- Cabrita R, Lauss M, Sanna A, et al. Tertiary lymphoid structures improve immunotherapy and survival in melanoma. *Nature* 2020;577:561–5.
- Vanhersecke L, Brunet M, Guégan J-P, et al. Mature tertiary lymphoid structures predict immune checkpoint inhibitor efficacy in solid tumors independently of PD-L1 expression. *Nat Cancer* 2021;2:794–802.
- Ruddle NH. High endothelial venules and lymphatic vessels in tertiary lymphoid organs: characteristics, functions, and regulation. *Front Immunol* 2016;7:491.
- Asrir A, Tardiveau C, Coudert J, et al. Tumor-associated high endothelial venules mediate lymphocyte entry into tumors and predict response to PD-1 plus CTLA-4 combination immunotherapy. *Cancer Cell* 2022;40:318–34.
- Binnewies M, Roberts EW, Kersten K, et al. Understanding the tumor immune microenvironment (TIME) for effective therapy. *Nat Med* 2018;24:541–50.
- Geissmann F, Jung S, Littman DR. Blood monocytes consist of two principal subsets with distinct migratory properties. *Immunity* 2003;19:71–82.
- Fei L, Ren X, Yu H, et al. Targeting the CCL2/CCR2 axis in cancer immunotherapy: one stone, three birds? *Front Immunol* 2021;12:771210.
- Gardner A, de Mingo Pulido Álvaro, Ruffell B. Dendritic cells and their role in immunotherapy. *Front Immunol* 2020;11:924.
- Baharlou H, Canete NP, Cunningham AL, et al. Mass cytometry imaging for the study of human Diseases-Applications and data analysis strategies. *Front Immunol* 2019;10:2657.
- Ali HR, Jackson HW, Zanutelli VRT, et al. Imaging mass cytometry and multiplatform genomics define the phenogenomic landscape of breast cancer. *Nat Cancer* 2020;1:163–75.

- 48 Keren L, Bosse M, Marquez D, *et al.* A structured Tumor-Immune microenvironment in triple negative breast cancer revealed by multiplexed ion beam imaging. *Cell* 2018;174:1373–87.
- 49 Schürch CM, Bhate SS, Barlow GL, *et al.* Coordinated cellular neighborhoods orchestrate antitumoral immunity at the colorectal cancer invasive front. *Cell* 2020;182:1341–59.
- 50 Wang X, Cho B, Suzuki K, *et al.* Follicular dendritic cells help establish follicle identity and promote B cell retention in germinal centers. *J Exp Med* 2011;208:2497–510.
- 51 Denton AE, Innocenti S, Carr EJ, *et al.* Type I interferon induces CXCL13 to support ectopic germinal center formation. *J Exp Med* 2019;216:621–37.
- 52 Cohen M, Giladi A, Barboy O, *et al.* The interaction of CD4⁺ helper T cells with dendritic cells shapes the tumor microenvironment and immune checkpoint blockade response. *Nat Cancer* 2022;3:303–17.
- 53 Fei L, Ren X, Yu H, *et al.* Targeting the CCL2/CCR2 axis in cancer immunotherapy: one stone, three birds? *Front Immunol* 2021;12:771210.
- 54 Tu MM, Abdel-Hafiz HA, Jones RT, *et al.* Inhibition of the CCL2 receptor, CCR2, enhances tumor response to immune checkpoint therapy. *Commun Biol* 2020;3:720.
- 55 Flores-Toro JA, Luo D, Gopinath A, *et al.* CCR2 inhibition reduces tumor myeloid cells and unmasks a checkpoint inhibitor effect to slow progression of resistant murine gliomas. *Proc Natl Acad Sci U S A* 2020;117:1129–38.